Nuclear Science and Techniques (2025) 36:4
https://doi.org/10.1007/s41365-024-01548-5

Positron annihilation study of defect formation and evolution in matrix graphite under He ion irradiation

Hong-Xia Xu[1] · Jian-Dang Liu[2] · Bang-Jiao Ye[2] · Zi-Wen Pan[2] · Jun Lin[1] · Jin-Liang Song[1] · Jian-Qing Cao[1] · Chao Yan[1] · Ying-Ping Hao[3] · Jin-Xing Cheng[4] · Qing-Bo Wang[4]

Received: 25 September 2023 / Revised: 21 March 2024 / Accepted: 7 April 2024 / Published online: 16 December 2024

Abstract

The stability of matrix graphite under neutron irradiation and in corrosive environments is crucial for the safe operation of molten salt reactors (MSRs). Raman spectroscopy and a slow positron beam were employed to investigate the effects of He ion irradiation fluences and subsequent annealing on the microstructure and defects of the matrix graphite. He ions with 500 keV energy and fluences ranging from 1.1×10^{15} ions/cm^2 to 3.5×10^{17} ions/cm^2 were used to simulate neutron irradiation at 300 K. The samples with an irradiation fluence of 3.5×10^{16} ions/cm^2 were subjected to isochronal annealing at different temperatures (573 K, 873 K and 1173 K) for 3 h. The Raman results revealed that the D peak gradually increased, whereas the intrinsic G peak decreased with increasing irradiation fluence. At the same irradiation fluence, the D peak gradually decreased, whereas the intrinsic G peak increased with increasing annealing temperature. Slow positron beam analysis demonstrated that the density or size of irradiation defects (vacancy type) increased with higher irradiation fluence, but decreased rapidly with increasing annealing temperature. The Raman spectral analysis of sample cross sections subjected to high irradiation fluences revealed the emergence of amorphization precisely at the depth where ion damage was most pronounced, whereas the surface retained its crystalline structure. Raman and positron annihilation analyses indicated that the matrix graphite exhibited good irradiation resistance to He ions at 300 K. However, vacancy-type defects induced by He ion irradiation exhibit poor thermal stability and can be easily removed during annealing.

Keywords Graphite · Positron annihilation · Irradiation · Raman spectrum

1 Introduction

Graphite has several advantages, including a low neutron absorption cross section, high thermal conductivity, and exceptional chemical stability, making it a prevalent neutron moderator material in reactors [1–3]. In addition to its role as a moderator and reflector, graphite is frequently employed as a structural material for the core and fuel elements in reactors [3–5]. It provides support for various components and establishes passages for coolant flow and control rods within the reactor gaps [5, 6]. Moreover, graphite serves as a matrix for spherical coated-particle fuel elements in high-temperature gas-cooled reactors (HTGRs) [3, 4].

Given that the typical design life of a nuclear reactor is approximately 40 years, the core structural materials in molten salt reactors (MSRs) inevitably endure harsh environments, including high temperatures, neutron irradiation, and coolant corrosion. The unique service conditions

This work was supported by the National Natural Science Foundation of China (Nos. 12005289, 52072397) and State Key Laboratory of Nuclear Detection and Electronics, University of Science and Technology of China (SKLPDE-KF-202316).

✉ Jian-Dang Liu
liujd@ustc.edu.cn

[1] Shanghai Institute of Applied Physics, Chinese Academy of Sciences, Shanghai 201800, China

[2] State Key Laboratory of Particle Detection and Electronics, University of Science and Technology of China, Hefei 230026, China

[3] Ruijin Hospital Affiliated to Shanghai Jiao Tong University School of Medicine, Shanghai 200025, China

[4] Beijing Institute of High Technology, Beijing 100094, China

in MSRs require that the fuel element matrix graphite not only exhibit excellent molten salt barrier properties but also demonstrate resistance to radiation. The formation and evolution of defects under irradiation can alter the pore structure of graphite, thereby affecting its barrier properties against molten salts. This situation can affect the safe operation and lifespan of reactors. Therefore, understanding the evolutionary patterns of these factors is crucial in guiding the design and operation of MSRs.

Significant research has been devoted to exploring the radiation properties of graphite over the years [1, 2, 7–11], resulting in the development of a preliminary radiation effect theory applicable to single crystals or highly oriented pyrolytic graphite (HOPG). When fast neutrons collide with carbon atoms in the graphite lattice, those receiving more than 25 eV of energy are displaced from the lattice, forming displaced atoms and vacancies. If the displaced carbon atom possesses sufficient energy, it can further dislodge other carbon atoms, initiating a cascade collision that generates a substantial number of dislocated atoms and vacancies within the graphite crystallites. Some of these dislocated atoms and vacancies may recombine quickly, whereas others contribute to the formation of irradiation defects, such as point defects, interstitial atom clusters, and vacancy clusters [1, 2]. Graphite crystals exhibit a highly anisotropic structure. Because of the sp^2 hybridization of carbon atoms on the graphite basal plane, the displaced atoms face challenges in fitting into the vacancies of the distorted basal plane. However, in the direction perpendicular to the basal plane, the bonding force (van der Waals force) between the carbon atoms is notably weak, facilitating the retention of off-site atoms between two adjacent basal planes of the lattice to form interstitial atoms. These self-interstitial atoms can aggregate and create in a new crystal plane, causing graphite to expand in the c direction and contract along the a-axis. The formation of numerous interstitial atomic groups, vacancy groups, and new crystal planes induces internal stress in the crystallites, leading to fracture of the graphite crystallites along the basal plane and a reduction in the crystallite size. With a continued increase in the irradiation dose, a sufficient number of vacancy clusters on the basal plane could cause its collapse, resulting in shrinkage in both the a and c directions. Further deterioration of the graphite structure eventually results in amorphization. Irradiation induces changes in the microstructure of graphite, leading to changes in its physical properties. The effect of radiation on graphite is intricately linked to factors such as the raw material type, proportion, molding and heat treatment processes, radiation dose, and radiation temperature [1, 2].

With the advancement of technology, current research and development is primarily directed toward fourth-generation reactors. Among them, MSRs have gained widespread attention from various countries owing to their advantages, such as water-free cooling, high-temperature operation, normal pressure, and intrinsic safety [12–18]. In an MSR, the coolant fluorine salt comes into direct contact with graphite, a brittle material with pores. Consequently, there is a demand for ultrafine particles and isotropic nuclear graphite that exhibit minimal dimensional changes after irradiation, low internal thermal stress, and excellent irradiation performance to adapt to the unique MSR service environment. As a result, the research and development of molten salt nuclear graphite primarily focuses on its high density (low porosity), high thermal conductivity, low elastic modulus, and low thermal expansion coefficient (minimal internal stress) [1].

Nuclear graphite used in gas-cooled reactors has been commercialized internationally (e.g., IG-110 and NBG-18). However, progress in nuclear graphite qualification for MSR applications has been slow. In the 1960 s, the Oak Ridge National Laboratory (ORNL) developed a special CGB graphite with a high degree of graphitization and anisotropy for the first liquid MSR experiment (MSRE) [19]. Although the pores of the CGB graphite are small ($< 0.4\,\mu m$), their anisotropy is high, and the size change caused by irradiation is significant and anisotropic (expanded along the c-axis and contracted along the basal plane). In contrast, during the development of HTGRs, isotropic matrix graphite A3-3 [3, 4] was developed and successfully applied to the spherical fuel elements of HTGRs. These components are expected to be useful for high-temperature fluoride salt-cooled reactors. Recently, Song et al. [20] proposed the use of mesophase carbon microbeads (MCMBs) as densifiers and isostatic pressing to prepare a new type of high-performance binderless nanoporous isostatic graphite (NPIG). The NPIG has shown superior performance compared to IG-110 and is anticipated to be used as a moderator and reflector material in MSRs. Currently, research on the irradiation properties of A3-3 matrix graphite is limited [21–25]. Delle et al. [21, 22] utilized neutron irradiation to study the effects of the radiation dose and annealing on the size, elasticity, modulus, resistivity, porosity, and other performance changes of A3-3 matrix graphite. Their findings suggest that recovery of graphite shrinkage caused by high-dose neutron irradiation is challenging, even after high-temperature annealing. Graphite samples irradiated at high temperatures and doses (10^{21} n/cm^2 equivalent dido nickel [EDN]) undergo changes in their physical properties upon annealing. Specifically, the resistivity and Young's modulus tend to decrease as the annealing temperature reaches 1673 K. Moreover, the observed trend exhibited an initial decline followed by a subsequent increase, ultimately leading to the formation of novel pores. This phenomenon occurs because of the accumulated internal stress induced by high-dose irradiation. Xu et al. [23–25] used Xe and Ar ions to irradiate matrix graphite and solid-phase densified matrix graphite at 300 K. They employed Raman, slow positron beam, and

nanoindentation test methods to investigate the changes in the crystal structure, defects, and mechanical properties of A3-3 matrix graphite after irradiation. Their results indicated that the defects generated in the matrix graphite under 1 dpa Xe ion irradiation significantly increased at 300 K, leading to amorphization and radiation hardening. Similarly, matrix graphite subjected to 1.47 dpa Ar ion irradiation also underwent amorphization and hardening. However, studies on the irradiation behavior of matrix graphite at high temperatures are scarce.

Owing to the high cost and challenges associated with neutron irradiation, this study used He ions to simulate neutrons. The matrix graphite for the coated-particle fuel element was irradiated at different fluences of 1.1×10^{15} ions/cm^2, 3.5×10^{16} ions/cm^2, and 3.5×10^{17} ions/cm^2 at 300 K. Samples irradiated at the specific fluence of 3.5×10^{16} ions/cm^2 were subsequently subjected to isothermal annealing at different temperatures. Raman spectroscopy and slow positron beam measurements were employed to investigate the irradiation defects of the fuel element matrix under He ion irradiation and the evolution of irradiation defects with changes in annealing temperature.

2 Experiment

The He ion irradiation experiment was conducted on a 4 MV linear accelerator platform at the Shanghai Institute of Applied Physics (SINAP), Chinese Academy of Sciences (CAS). A3-3 matrix graphite samples were irradiated with 500 keV He ions and fluences of 1.1×10^{15} ions/cm^2, 3.5×10^{16} ions/cm^2, and 3.5×10^{17} ions/cm^2 at 300 K. Samples with an irradiation fluence of 3.5×10^{16} ions/cm^2 underwent isochronous 3-h annealing experiments at temperatures of 573 K, 873 K, and 1173 K under an Ar protective atmosphere. Table 1 presents detailed information on the samples used in the irradiation experiment.

The primary raw materials for the A3-3 matrix graphite used in the experiment were 64% natural graphite, 16% artificial graphite, and 20% phenolic resin as a binder. The sample was subjected to cold isostatic pressing, followed by carbonization and graphitization, resulting in a nearly isotropic polycrystalline material with a porosity of approximately 18% and a density of 1.73 g/cm^3 [25, 26]. Each sample is 10 mm in diameter and has a thickness of 1 mm. Before irradiation, the sample was polished with 2000 grit SiC sandpaper, ultrasonically cleaned with alcohol, dried, and stored in a 300 K vacuum incubator.

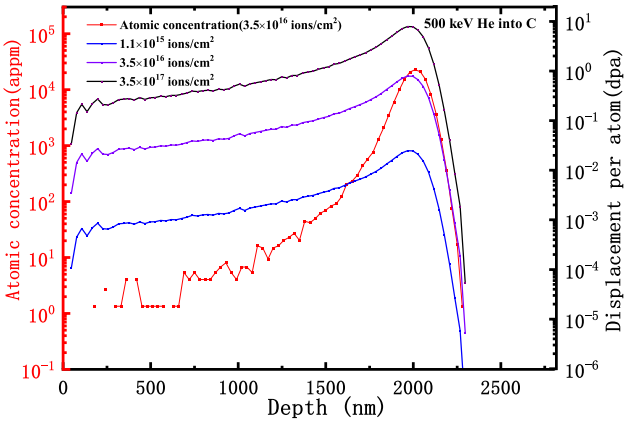

Fig. 1 (Color online) Depth profile of displacements per atom (dpa) and He ion concentration ($_{3.5}$) in A3-3 matrix graphite irradiated with 500 keV He ions to various fluences calculated by SRIM

The Monte Carlo simulation program stopping and range of ions in matter (SRIM) [27] was employed to simulate the distribution of He ions and the irradiation damage induced by the 500 keV He ions in the matrix graphite. The dislocation threshold energy of the carbon atoms was set to 25 eV, and the atomic density was 8.67×10^{22} atoms/cm^3 (1.73 g/cm^3). The damage depth caused by 500 keV He ions in the graphite was approximately 2.2 μm, with irradiation damage peaks formed at approximately 2 μm beneath the surface. The corresponding peak damages for 10^{15} ions/cm^2, 3.5×10^{16} ions/cm^2, and 3.5×10^{17} ions/cm^2 were 0.025 dpa, 0.79 dpa, and 7.9 dpa, respectively. Figure 1 illustrates the distribution of the irradiation damage and He

Table 1 Details of samples for He ion irradiation

No.	Irradiation temperature (K)	Irradiation fluence (ions/cm^2)	Displacements per atom (dpa)	Annealing temperature (K)	Annealing duration (h)
1	300	0	0	–	–
2	300	1.1×10^{15}	0.025	–	–
3	300	3.5×10^{16}	0.79	–	–
4	300	3.5×10^{16}	0.79	573	3
5	300	3.5×10^{16}	0.79	873	3
6	300	3.5×10^{16}	0.79	1173	3
7	300	3.5×10^{17}	7.9	–	–

ion concentration in the sample with depth calculated using SRIM.

Raman spectroscopy, which is known for its nondestructive nature and high sensitivity to the bonding mode of graphite, has been extensively applied in the microstructural analysis of graphite materials before and after irradiation [9–11, 28–36]. The samples were tested using a LABRAM HR800 laser Raman instrument with a laser power of 100 mW and wavelength of 531.5 nm.

Slow positron beams are renowned for their exceptionally high sensitivity in detecting atomic-sized defects on material surfaces or interfaces, offer single and continuously adjustable positron injection energy, enable nondestructive testing, and have become instrumental in studying defect evolution in nuclear materials during irradiation research [37–42]. In this study, samples were examined using a slow positron beam measurement system at the State Key Laboratory of Nuclear Detection and Electronics, University of Science and Technology of China (USTC) [23, 24]. The energy of the monoenergetic positron beam could be continuously adjusted within the range of 0–30 keV, and the vacuum level of the target chamber was maintained at 10^{-5} Pa. A high-purity Ge detector was used to measure the Doppler broadening spectrum of 1.33 MeV gamma photons with an energy resolution of approximately 1.85 keV. After injection of positrons with a specific energy into the sample, they undergo processes such as excitation, ionization, rapid thermalization, diffusion, and migration before annihilation with the electrons within the sample. Changes in the microstructure caused by irradiation can affect the distribution of electron density and momentum, resulting in a significant alteration in the positron annihilation parameters. Because the positron energy after thermalization is minimal (approximately 0.025 eV at 300 K), the Doppler broadening of positrons to annihilate γ photons is primarily influenced by the annihilation electron momentum. Experimental measurements were conducted at 300 K, with the channel width set at 24.51 eV and net counts in the single-peak area exceeding 10^5. The linear parameters *S* and *W* are defined as the ratio of the counts in the central region (510.24–511.76 keV), and two wing regions (515.16–516.66 keV and 505.34–506.84 keV) to the total counts of the entire region (504.20–517.80 keV) in the annihilation γ-photon Doppler broadening spectrum. These parameters reflect the annihilation information concerning electrons with low and high momentum.

3 Results and discussion

3.1 Raman spectroscopy

The graphite samples were irradiated with 500 keV He ions at different fluences, and the subsequent changes were evaluated using Raman spectroscopy, as illustrated in Fig. 2. The initial Raman analysis of the pre-irradiated matrix graphite samples revealed distinct peaks at 1360 cm^{-1} and 1580 cm^{-1}, corresponding to the D peak representing defects and the intrinsic G peak representing atomic vibration in the basal plane, respectively [9, 10]. The G peak exhibited a significantly higher intensity than the D peak, indicating a high degree of graphitization and an ordered crystal structure in the A3-3 matrix graphite.

Following low-fluence (0.025 dpa) He ion irradiation, slight changes were observed in the D and G peak intensities of the matrix graphite. The D peak exhibited a slight enhancement and broadening, indicating the introduction of vacancy defects owing to He ion irradiation. With an increased fluence of 0.79 dpa, the intensity of the D peak gradually increased, whereas the intrinsic G peak intensity decreased. The intensities of these two peaks approached each other, indicating a continuous increase in defects with increasing He ion fluences. At a fluence of 7.9 dpa, both the D and G peaks exhibited further broadening, with the D peak becoming dominant. However, these two peaks remained distinguishable, and no characteristic signs of amorphization were observed on the surfaces of the post-irradiation samples [34, 35]. Literature [30, 31] suggests that the critical fluence of amorphization in graphite under He ion irradiation is approximately 1 dpa. However, Avilkina [33] found that the critical fluence exceeded 1 dpa when other ions were used. This observation implies that, even after irradiation with 1×10^{17} ions/cm^2 He ions, the surface of the matrix graphite preserved its crystal structure without undergoing amorphization. In contrast, our previous reports on Xe-ion-irradiated A3-3 matrix graphite [23] indicated that a fluence of 1×10^{14} ions/cm^2 can lead to amorphization, resulting in a bulging Raman spectrum in which the D and G peaks are

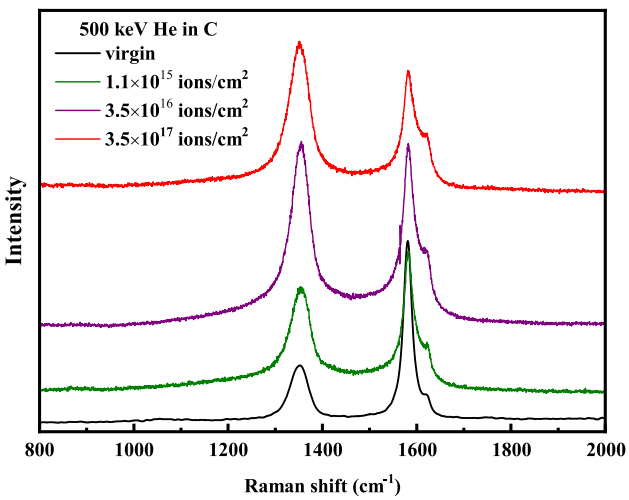

Fig. 2 (Color online) Raman spectrum of A3-3 matrix graphite irradiated with 500 keV He ions to various fluences

indistinguishable. This discrepancy highlights that Xe ions can significantly damage the crystal structure of the matrix graphite at lower irradiation fluences, while the A3-3 surface structure remains intact even at He ion irradiation fluences three orders of magnitude higher than those of the Xe ions. Therefore, the A3-3 matrix graphite demonstrates robust resistance to He ion irradiation.

In accordance with the calculated distribution of displacements per atom (dpa) with depth in the A3-3 matrix graphite, as depicted in Fig. 1, the peak damage depth is estimated to be approximately 2 μm beneath the surface. Consequently, we selected the matrix graphite irradiated at a fluence of 3.5×10^{16} ions/cm^2 to provide a clear illustration of the irradiation effects. Figure 3 shows the structure of the matrix graphite cross section, characterized by Raman spectra at various depths. The D and G peaks initially broadened as the depth increased and became nearly indistinguishable at a depth of 1.8 μm beneath the surface. This observation suggests that the degree of irradiation damage reaches its maximum and the matrix graphite approaches amorphization at this depth. Subsequently, the D and G peaks become independent and distinguishable at a depth of 2.2 μm, resembling the shapes observed in the surface Raman spectrum. Furthermore, as the depth increased to approximately 2.6 μm, the D and G peaks gradually reverted to their original pre-irradiation states. This indicates that the maximum depth of damage should be in the range of 1.8−2.2 μm, which is consistent with the results obtained from the SRIM simulation.

To investigate the annealing effect, we employed 500 keV He ions to irradiate the matrix graphite to a constant fluence of 3.5×10^{16} ions/cm^2. Subsequently, the irradiated samples were isochronously annealed at different temperatures, and the Raman spectrum of the annealed samples were measured. The results are shown in Fig. 4.

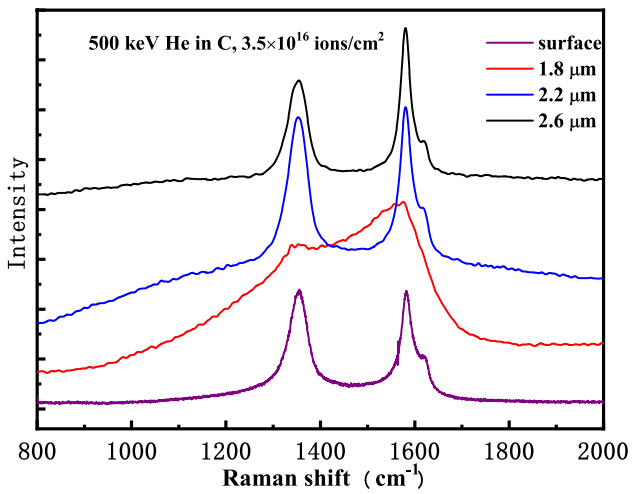

Fig. 3 (Color online) Raman spectrum of A3-3 matrix graphite cross section irradiated with 500 keV He ion to a fluence of $3.5 \times$

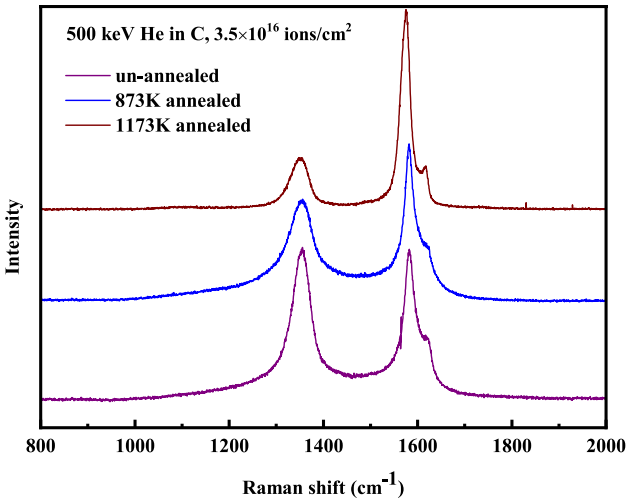

Fig. 4 (Color online) Raman spectrum of A3-3 matrix graphite irradiated with 500 keV He ion to a fluence of $_3$ and annealed at various temperatures

Observations reveal that the heights of the D and G peaks in the irradiated and unannealed samples are similar, indicating the presence of numerous irradiation defects in the matrix graphite. After annealing at 873 K, the D peak decreases, whereas the G peak increases, indicating the recovery of irradiation defects under the annealing conditions. Further annealing at 1173 K led to a continued decrease in the D peak and an increase in the G peak, with the Raman spectrum of the matrix becoming consistent with that of pre-irradiated matrix graphite. This indicates the complete disappearance of the vacancy defects generated by irradiation and the recovery of the matrix graphite after high-temperature annealing. This recovery process is consistent with the mechanism proposed by Delle et al. [21] for the formation and evolution of defects in A3-3 matrix graphite under neutron irradiation. According to their findings, low-temperature irradiation primarily results in the formation of vacancy-type defects, such as mono-vacancies, di-vacancies, and small vacancy clusters, which can be eliminated through annealing. When irradiating A3-3 matrix graphite in the temperature range of 573–873 K, neutron irradiation induces damage such as interstitial clusters and vacancies. These defects can reduce the size of the large interstitial clusters and increase their number through annealing, thereby facilitating vacancy recombination. At higher irradiation temperatures, small interstitial groups were formed between the crystal planes, which migrated and aggregated to form clusters. These interstitial clusters are highly stable and exhibit low recombination with vacancy clusters even at high temperatures. However, under higher neutron fluence irradiation or at higher irradiation temperatures, vacancy clusters may collapse or migrate to the grain boundaries. This explains why high-temperature annealing

after irradiation only partially recovers the physical properties of A3-3 matrix graphite. Based on the aforementioned analysis, it is presumed that the defects generated in the A3-3 matrix graphite irradiated with He ions consisted mainly of mono-vacancies, di-vacancies, and small vacancy clusters, which readily recombined during annealing.

3.2 Slow positron beam

At 300 K, A3-3 matrix graphite was irradiated with 500 keV He ions at various fluences. Subsequently, the *S*-parameters of A3-3 matrix graphite were measured using slow positron beams after irradiation and annealing at various temperatures. The *S*–*E* curves representing the change in defects with positron energy are shown in Figs. 5 and 6. The mean implantation depth of the positrons, denoted by *Z* (nm), can be readily estimated using the incident positron energy *E* (keV) and the density of the target materials ρ (g/cm^3), as expressed by the equation $Z = (40/\rho) \times E^{1.6}$ [37–40]. The vertical axis represents the measured *S*-parameters. Different microstructural layers exhibit distinct electron momentum or density distributions, resulting in significant variations in the measured *S*-parameters.

Figure 5 illustrates the *S*–*E* curves of the post-irradiation samples subjected to different fluences at 300 K, as measured using a slow positron beam. Common features were observed among all post-irradiation samples in Fig. 5: the *S*-parameter is high when the positron energy (*E*) is very low and tends to stabilize after reaching a certain value. This behavior is attributed to the shallow injection depth of the positrons in the sample (< 70 nm) when the positron injection energy is relatively low (*E* < 2 keV). Partially thermalized positrons diffuse to the surface and interact

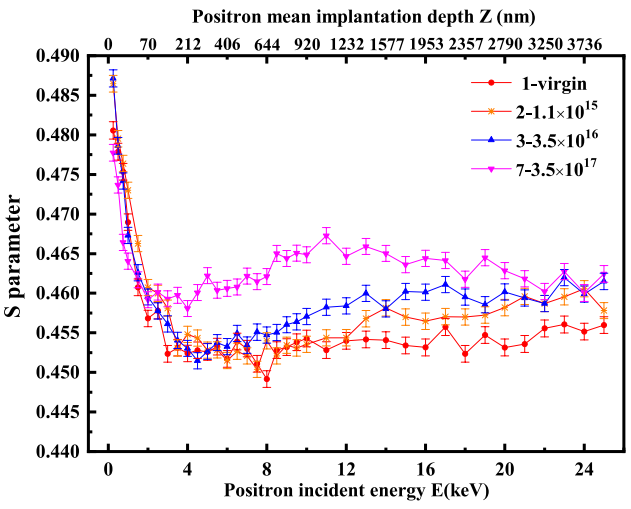

Fig. 5 (Color online) *S*-parameter as a function of positron incidence energy or mean implantation depth (*S*–*E* curve) in A3-3 matrix graphite irradiated to various fluences

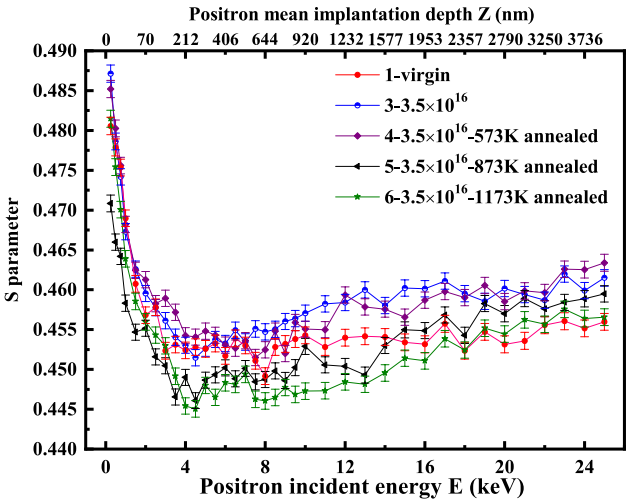

Fig. 6 (Color online) *S*-parameter as a function of positron incidence energy or mean implantation depth (*S*–*E* curve) in He ion irradiated A3-3 graphite annealed at various temperatures

with surface electrons, resulting in higher *S*-parameters. In contrast, at high positron energies (*E* > 24 keV), where the injection depth in the sample is approximately 3.7 μm (significantly greater than the 2.2 μm depth of the irradiation damage layer calculated by SRIM), most positrons diffuse and annihilate with electrons in the matrix. Consequently, the *S* value of the irradiated sample approaches that of the pre-irradiated sample, indicating a stable bulk annihilation parameter value of 0.455. For positron energies within the range 2 keV < *E* < 24 keV, the *S*-parameter exhibits regular changes with increasing irradiation fluence, primarily reflecting alternations in the positron annihilation characteristics within the irradiation defect layer.

At 300 K, when the He ion irradiation fluence is 1.1×10^{15} ions/cm^2, the *S*-parameters show minimal changes compared with the pre-irradiation sample. As the irradiation fluence increases from 1.1×10^{15} ions/cm^2 to 3.5×10^{16} ions/cm^2, the *S*-parameters of the defect layer slightly increase. Upon further increasing the irradiation fluence to 3.5×10^{17} ions/cm^2, the *S*-parameters of the defect layer exhibit a significant increase compared to those of the pre-irradiation sample. This can be explained by the fact that under low-fluence irradiation, the density or size of the vacancy-type defects generated in the samples is relatively small. A slight increase in the D peak in the Raman spectrum shown in Fig. 3 also supports this observation. However, under high-fluence irradiation, the density or size of the vacancy-type defects in the sample increase sharply, resulting in a pronounced increase in the D peak intensity in the Raman spectrum. Its intensity even surpasses that of the intrinsic G peak of graphite, making the D peak a dominant feature. It is worth noting that when the implantation depth of the positrons is relatively shallow (70 nm < *Z* < 644 nm),

corresponding to the initial portion of the He ion range, the change in the *S*-parameters for the irradiated samples is less pronounced compared with the pre-irradiation samples. However, as the implantation depth of the positrons increases toward deeper regions (644 nm < Z < 2357 nm) approaching the end of the He ion range, the change in the *S*-parameters of the irradiated samples became more significant. This observation suggests that large defects or a higher density of defects are generated toward the end of the He ion range, which is consistent with our earlier findings regarding nuclear stopping and the formation of large damage cascades. Although the matrix graphite was irradiated at 1×10^{17} ions/cm^2, the Raman analysis results show that the surface of the matrix graphite has not yet been amorphized, indicating that the A3-3 matrix graphite is very resistant to He ion irradiation at 300 K. Hu et al. [41] reported that the *S*-parameter of IG-110 nuclear graphite irradiated with He ions varied with irradiation fluence. They also observed that when the He ion irradiation fluence was 1×10^{15} ions/cm^2, the *S*-parameter of IG-110 did not change significantly. However, when the irradiation fluence was increased to 1×10^{16} ions/cm^2, the *S*-parameters of IG-110 showed significant variation. By comparing these results, we found a similar trend between the defect evolution in IG-110 graphite irradiated with He ions and changes in the *S*-parameters observed in A3-3 matrix graphite after He ion irradiation at 300 K. These findings indicate a similarity between the two materials. Therefore, the experimental results demonstrate that both IG-110 and A3-3 matrix graphite exhibit good resistance to He ion irradiation at 300 K.

Isochronous annealing experiments were conducted on post-irradiation samples with an irradiation fluence of 3.5×10^{16} ions/cm^2, and the *S*–*E* curves were measured using slow positron beams, as depicted in Fig. 6. The results indicate that the *S*-parameters of the post-irradiation sample exhibited an increasing trend compared to those of the pre-irradiation sample, indicating the introduction of vacancy-type defects, such as mono-vacancies, di-vacancies, and small vacancy clusters in the matrix graphite due to irradiation.

For the post-irradiation sample annealed at 573 K, the *S*-parameter was slightly lower than that of the post-irradiation sample without annealing, indicating that some vacancy-type defects induced by He ion irradiation were mitigated by annealing. As the annealing temperature was further increased to 873 K, the *S*-parameters in the irradiated damage layer decreased significantly and approached those of the pre-irradiated sample. This indicates that when the annealing temperature reached 873 K, the vacancy-type defects caused by irradiation were nearly completely restored. By increasing the annealing temperature to 1173 K, the *S*-parameter exhibited only slight changes compared with that of the post-irradiation sample annealed at 873 K. This observation further confirms that the vacancy-type defects generated by He ion irradiation were essentially eradicated by annealing. The Raman spectrum (Fig. 4) also demonstrates that as the annealing temperature increases, the intensity of the defect D peak decreases, while the characteristic G peak of graphite increases and returns to the pre-irradiation level. This finding aligns with the conclusion drawn by Delle et al. [21], which suggests that irradiation-induced vacancy-type defects, such as mono-vacancies, di-vacancies, and small vacancy clusters in graphite can be easily eliminated by annealing. Shi et al. [42] employed C ions to irradiate ETU10 graphite and discovered that the two temperatures for repairing point defects caused by low-fluence irradiation were approximately 450 K and 700 K, respectively. Furthermore, the thermal stability of large vacancy clusters V_6 induced by high-fluence irradiation was found to be considerably robust because it was challenging to eliminate them, even at a high temperature of 1400 K. Based on the aforementioned analysis, the vacancy-type defects introduced by He ion irradiation in A3-3 matrix graphite at 300 K are primarily mono-vacancies, di-vacancies, and small vacancy clusters. These vacancy-type defects exhibit poor thermal stability and can be readily eliminated by annealing. Therefore, A3-3 matrix graphite demonstrates excellent resistance to He ion irradiation at 300 K.

4 Conclusion

Raman spectroscopy and a slow positron beam were employed at 300 K to investigate the impact of He ion fluence on the generation of point defects in A3-3 matrix graphite. Changes in the intensities of the Raman D and G peaks, as well as the SE curves, were obtained. The main conclusions are as follows:

(1) When the He ion irradiation fluence is below 10×10^{16} ions/cm^2, the irradiation damage to the A3-3 matrix graphite is minimal. The D peak broadens slightly and its intensity increase. The *S*-parameter of the post-irradiation sample shows no significant change compared with that of the pre-irradiated sample.

(2) When the He ion irradiation fluence exceeds 10×10^{16} ions/cm^2, irradiation damage in the A3-3 matrix graphite (approximately 2 μm) occurs, characterized by the presence of vacancy-type defects, such as mono-vacancies, di-vacancies, and small vacancy clusters. As the irradiation fluence increased, the concentration of vacancy-type defects in the damaged layer increased, leading to the enhancement of the D peak and weakening of the G peak in the Raman spectrum. Consequently, the *S*-parameter increases rapidly. Furthermore, Raman spectral analysis of the cross section

revealed the occurrence of amorphization at the depth of maximum irradiation damage.

(3) Even when the He ion irradiation fluence reached 10×10^{17} ions/cm^2, the surface of the A3-3 matrix graphite did not undergo amorphization. This observation indicates that the A3-3 matrix graphite exhibits excellent resistance to He ion irradiation at 300 K.

(4) The thermal stability of vacancy-type defects, such as mono-vacancies, di-vacancies, and small vacancy clusters induced by He ion irradiation is notably poor. Partial recovery occurs when the annealing temperature is 573 K, and most of these vacancy-type defects are recovered as the annealing temperature increases to 873 K. With the recovery of the vacancy-type defects, the intensity of the D peak and the *S*-parameters decreased rapidly, and the crystal structure of the matrix graphite returned to its pre-irradiation level.

Authors' contributions All authors contributed to the study conception and design. Material preparation, data collection and analysis were performed by H-XX, Z-WP, CY and Y-PH. The first draft of the manuscript was written by H-XX, and all authors commented on previous versions of the manuscript. All authors read and approved the final manuscript.

Declarations

Conflict of interest The authors declare that they have no conflict of interest.

References

1. T.D. Burchell, *Carbon Materials for Advanced Technologies* (Pergamon, Oak Ridge National Laboratory, 1999). https://doi.org/10.1016/B978-0-08-042683-9.X5000-6
2. G.B. Engle, B.T. Kelly, Radiation damage of graphite in fission and fusion reactor systems. Nucl. Mater. **122**, 122–129 (1984). https://doi.org/10.1016/0022-3115(84)90582-8
3. Advances in high temperature gas cooled reactor fuel technology. IAEA-TECDOC-1674, 978-92-0-186810-7, June, Vienna (Austria) (2012)
4. C.H. Tang, Y.P. Tang, J.G. Zhu et al., Design and manufacture of the fuel element for the 10 MW high temperature gas-cooled reactor. Nucl. Eng. Des. **218**, 91–102 (2002). https://doi.org/10.1016/S0029-5493(02)00201-7
5. Y. Zhong, X. Yang, D. Ding et al., Numerical study of the dynamic characteristics of a single-layer graphite core in a thorium molten salt reactor. Nucl. Sci. Tech. **29**, 141 (2018). https://doi.org/10.1007/s41365-018-0488-8
6. L. He, C.G. Yu, R.M. Ji et al., Development of a dynamics model for graphite moderated channel type molten salt reactor. Nucl. Sci. Tech. **30**, 18 (2019). https://doi.org/10.1007/s41365-018-0541-7
7. G.E. Bacon, B.E. Warren, X-ray diffraction studies of neutron-irradiated graphite. Acta Cryst. **9**, 1029 (1956). https://doi.org/10.1107/S0365110X56002989
8. W. Qi, Z.T. He, B.L. Zhang et al., Behaviors of fine (IG-110) and ultra-fine (HPG-510) grain graphite irradiated by 7 MeV Xe^{26+} ions. Nucl. Sci. Tech. **28**, 144 (2017). https://doi.org/10.1007/s41365-017-0292-x
9. K. Niwase, K. Nakamura, T. Shikama et al., On the amorphization of neutron irradiated graphite. Nucl. Mater. **170**, 106–108 (1990). https://doi.org/10.1016/0022-3115(90)90332-H
10. A.C. Ferrari, J. Robertson, Interpretation of Raman spectra of disordered and amorphous carbon. Phys. Rev. B **61**, 14095–14107 (2000). https://doi.org/10.1103/PhysRevB.61.14095
11. Q.T. Lei, Z.T. He, W. Qi et al., Irradiation-induced mixing of Na and K in graphite in molten salt reactor: an estimation based on ion beam irradiation. Nucl. Instrum. Methods B **450**, 100–107 (2019). https://doi.org/10.1016/j.nimb.2018.08.018
12. J. Serp, M. Allibert, O. Benes et al., The molten salt reactor (MSR) in generation IV: overview and perspectives. Prog. Nucl. Energy **77**, 308–319 (2014). https://doi.org/10.1016/j.pnucene.2014.02.014
13. The U.S. DOE Nuclear Energy Research Advisory Committee and the Generation IV International Forum, A technology Roadmap for Generation IV Nuclear Energy Systems, GIF-002-00 (2002)
14. C. Forsberg, The advanced high-temperature reactor: high-temperature fuel, liquid salt coolant, liquid-metal-reactor plant. Prog. Nucl. Energy **47**, 32–43 (2005). https://doi.org/10.1016/j.pnucene.2005.05.002
15. K. Furukawa, K. Arakawa, L.B. Erbay et al., A road map for the realization of global-scale thorium breeding fuel cycle by single molten-fluoride flow. Energy Convers. Manag. **49**, 1832–1848 (2008). https://doi.org/10.1016/j.enconman.2007.09.027
16. Q. Huang, Q.T. Lei, H. Tang et al., Fracture resistance of imperfect filler particles within nuclear graphite during irradiation. Nucl. Instrum. Methods B **464**, 123–127 (2020). https://doi.org/10.1016/j.nimb.2019.12.022
17. M.H. Jiang, H.J. Xu, Z.M. Dai, Advanced fission energy program-TMSR nuclear energy system. Bull. Chin. Acad. Sci. **27**, 366–374 (2012)
18. Y. Wang, Y. Ma, N.B. Jiang et al., Preliminary analysis of the irradiation deformation of a typical molten salt reactor graphite component. Prog. Nucl. Energy **128**, 105009J (2024). https://doi.org/10.1016/j.pnucene.2023.105009
19. E.S. Bettis, S.S. Kirslis, W.H. Cook et al., Graphite behavior and its effect on MSBR performance, Oak Ridge National Laboratory, ORNL-2136 (1969)
20. J.L. Song, Y.L. Zhao, J.P. Zhang et al., Preparation of binderless nanopore-isotropic graphite for inhibiting the liquid fluoride salt and Xe135 penetration for molten salt nuclear reactor. Carbon **79**, 36–45 (2014). https://doi.org/10.1016/j.carbon.2014.07.022
21. Irradiation damage in graphite due to fast neutrons in fission and fusion systems, IAEA-TEC-DOC-1154, Vienna, Austria (2000)
22. C.H. Tang, Z.Q. Li, Y.W. Zou et al., Irradiation testing of matrix material for spherical HTR-10 fuel elements. Nucl. Eng. Des. **238**, 2886–2892 (2008). https://doi.org/10.1016/j.nucengdes.2008.01.021
23. H.X. Xu, J. Lin, J.J. Li et al., Characterization the microstructure and defects of matrix graphite irradiated with Xe ions. Nucl. Instrum. Methods B **406**, 638–642 (2017). https://doi.org/10.1016/j.nimb.2017.03.159
24. H.X. Xu, J. Lin, Z.Y. Zhu et al., Slow positron beam study on defects induced by Xe ions irridiation in matrix graphite of fuel elements. Nucl. Tech. **45**, 100204 (2022). https://doi.org/10.11889/j.0253-3219.2022.hjs.45.100204. (**in Chinese**)
25. L.J. Xu, H.R. Wang, J. Lin et al., The effect of Ar ion beam irradiation on mesocarbon microbead-densified graphite as the matrix of fuel elements in molten salt nuclear reactors. New Carbon Mater. **33**, 268–275 (2018). https://doi.org/10.19869/j.ncm.1007-8827.2018.03.006
26. H.X. Xu, J. Lin, Y.J. Zhong et al., Characterization of molten 2LiF-BeF_2 salt impregnated into graphite matrix of fuel elements

for Thorium molten salt reactor. Nucl. Sci. Tech. **30**, 74 (2019). https://doi.org/10.1007/s41365-019-0600-8
27. J.F. Ziegler, M.D. Ziegler, J.P. Biersack, SRIM-The stopping and range of ions in matter. Nucl. Instrum. Methods B **268**, 1818–1823 (2010). https://doi.org/10.1016/j.nimb.2010.02.091
28. B.S. Elman, M.S. Dresselhaus, G. Dresselhaus et al., Raman scattering from ion-implanted graphite. Phy. Rev. B **24**, 1027–1034 (1981). https://doi.org/10.1103/PhysRevB.24.1027
29. J.B. Malherbe, O.S. Odutemowo, E.G. Njoroge et al., Ion bombardment of glassy carbon. Vacuum **149**, 19–22 (2018). https://doi.org/10.1016/j.vacuum.2017.11.006
30. T. Tanabe, T. Maruyama, M. Iseki et al., Radiation damage of graphite-degradation of material parameters and defect structures. Fusion Eng. Des. **29**, 428–434 (1995). https://doi.org/10.1016/0920-3796
31. K. Niwase, Raman spectroscopy for quantitative analysis of point defects and defect clusters in irradiated graphite. Int. J. Spectrosc. **2012**, 197609 (2012). https://doi.org/10.1155/2012/197609
32. S.J. Hang, Z. Moktadir, H. Mizuta, Raman study of damage extent in graphene nanostructures carved by high energy helium ion beams. Carbon **72**, 233–241 (2014). https://doi.org/10.1016/J.CARBON.2014.01.071
33. V.S. Avilkina, N.N. Andrianova, A.M. Borisov et al., Energy and temperature dependences of ion-induced electron emission from polycrystalline graphite. Nucl. Instrum. Methods B **269**, 995–998 (2011). https://doi.org/10.1016/j.nimb.2010.12.030
34. A.C. Ferrari, J. Robertson, Interpretation of Raman spectra of disordered and amorphous carbon. Phys. Rev. B **61**, 14095–14107 (2000). https://doi.org/10.1103/PhysRevB.61.14095
35. S. Ishiyama, T.D. Burchell, J.P. Strizak et al., The effect of high fluence neutron irradiation on the properties of a finegrained isotropic nuclear graphite. Nucl. Mater. **230**, 1–7 (1996). https://doi.org/10.1016/0022-3115(96)00005-0
36. H.Y. Zhang, Z. He, J.L. Song et al., Characterization of the effect of He+ irradiation on nanoporousisotropic graphite for molten salt reactors. Nucl. Eng. Technol. **52**, 1243–1251 (2020). https://doi.org/10.1016/j.net.2019.11.033
37. F.A. Selim, Positron annihilation spectroscopy of defects in nuclear and irradiated materials a review. Mater. Charact. **174**, 110952 (2021). https://doi.org/10.1016/0022-3115(91)90061-B
38. J.J. Shi, W.Z. Zhao, Y.C. Wu et al., Characterization of proton-irradiated Chinese A508–3-type reactor pressure vessel steel by slow positron beam, TEM, and nanoindentation. Nucl. Instrum. Methods B **443**, 2–69 (2019). https://doi.org/10.1016/j.nimb.2019.01.04
39. S.X. Jin, X.Y. Lian, T. Zhu et al., Irradiation evolution of Cu precipitates in Fe1.0Cu alloy studied by positron annihilation spectroscopy. Nucl. Mater. **499**, 65–70 (2018). https://doi.org/10.1016/j.jnucmat.2017.11.011
40. Z.Q. Chen, M. Maekawa, S. Yamamoto et al., Evolution of voids in Al+ implanted ZnO probed by a slow positron beam. Phys. Rev. B **69**, 035210 (2004). https://doi.org/10.1103/physrevb.69.035210
41. Z. Hu, Z. Li, Z. Zhou et al., Positron and thermal desorption studies on He ion implanted nuclear graphite. Phys. Conf. Ser. **505**, 012014 (2014). https://doi.org/10.1088/1742-6596/505/1/012014
42. C.Q. Shi, H. Schut, Z.C. Li, Thermal annealing of C ion irradiation defects innuclear graphite studied by positron annihilation. Phys. Conf. Ser. **674**, 012019 (2016). https://doi.org/10.1088/1742-6596/674/1/012019